Quadrature Wavelength Scanning Interferometry

GIUSEPPE MOSCHETTI[1,2], ALISTAIR FORBES[1], RICHARD K LEACH[3], XIANG JIANG[2], AND DANIEL O'CONNOR[1]

[1] National Physical Laboratory, Hampton Road, Teddington, Middlesex, TW11 0LW, UK
[2] Centre for Precision Technologies, University of Huddersfield, Huddersfield, West Yorkshire, HD1 3DH, UK
[3] Manufacturing Metrology Team, University of Nottingham, Nottingham, NG7 2RD, UK
[*] Corresponding author: giuseppe.moschetti@npl.co.uk

Compiled June 20, 2016

A novel method to double the measurement range of wavelength scanning interferometery (WSI) is described. In WSI the measured optical path difference (OPD) is affected by a sign ambiguity, *i.e.* from an interference signal it is not possible to distinguish whether the OPD is positive or negative. The sign ambiguity can be resolved by measuring an interference signal in quadrature. A method to obtain a quadrature interference signal for WSI is described and a theoretical analysis of the advantages is reported. Simulations of the advatanges of the technique and of signal errors due to non-ideal quadrature are discussed. The analysis and simulation are supported by experimental measurements to show the improved performances.

OCIS codes: *(120.3180) Interferometry, (120.2650) Fringe analysis, (120.3940) Metrology, (120.6650) Surface measurements, figure*

1. INTRODUCTION

Interferometry is a widely-used technique to measure displacement and, when combined with an optical microscope, can allow the extraction of surface height information from interference fringe data. Interferometers commonly used to measure surface topography are phase shifting [1, 2], white light [2, 3] and wavelength scanning [4, 5]. Each type of interferometer has certain advantages and disadvantages concerning the acquisition of the fringe data and the extraction of surface topography data.

In phase shifting interferometry (PSI) fringe data is obtained by modulating the optical path difference between the measurement and the reference arm by a known amount and recording the intensity values [6, 7]. The modulation is typically achieved by mechanically scanning the reference mirror (or sample), and it requires a highly stable system with precision motion control. Another disadvantage of PSI is the 2π ambiguity that is encountered when measuring discontinuous surfaces with step heights larger than half the wavelength of the light used [8]. Dual-wavelength methods allow one to extend the unambiguos measurement range to typical distances of few micrometres but do not avoid it [9, 10].

Coherence scanning interferometry (CSI) (also known as white light interferometry) is another well-established technique used to obtain surface topography [2]. Due to the low-coherence length of the broadband light, interference fringes only become visible when the optical path length of the measurement and reference arms are close to being equal. Thus, the optical path must again be modulated, typically via a mechanical scan, in order to record fringe data. The surface height can be estimated from the fringe data as the location at which the envelope of the interference signal reaches the maximum intensity value. Further resolution improvement is possible by estimating the surface height from the phase of the interference signal and solving for the fringe order through the envelope peak [11–13]. The advantage of CSI technique over PSI is removal of 2π phase ambiguity. The main disadvantage of CSI is the need for mechanical scanning over the entire range of heights present in the sample, therefore, the measurement time in CSI becomes directly proportional to the range of the surface heights which is often unknown *a priori*. Both phase shifting and white light interferometry can achieve sub-nanometre axial resolution [2].

Wavelength scanning interferometry (WSI) is a technique where fringe data is obtained by introducing a phase shift in the interference pattern via a wavelength sweep (that is linear in wavenumber) of the narrow bandwidth interfering light [5, 14]. The main advantage of WSI over CSI is that there is no need for mechanically scanning the sample due to the long coherence length of the illumination. However, in WSI the measurement range is limited by the objective lens depth of field. At the position where the measurement and reference arm have equal optical path length, *i.e.* zero optical path difference (OPD), the interference is constructive for all the scanned wavelengths, while away from the zero OPD position the recorded fringe intensities

as a function of the wavenumbers has a frequency that is proportional to the OPD. Thus, by calculating the frequency of the recorded fringe pattern, it is possible to calculate the OPD and, therefore, determine the surface distance from the zero OPD position. The largest OPD that is possible to measure is limited by either the coherence length of each scanned wavelength (limit for very low NA systems) or by the objective depth of field (usually the limit for medium to high NA systems). The shortest OPD that is possible to measure is limited by the fringe pattern processing algorithm: close to the zero OPD the fringe pattern approaches constructive interference for all wavenumbers and therefore a frequency of almost zero. Phase demodulation algorithms performance degrades for fringe patterns that have samples over less than a period since it becomes difficult to spectrally filter the interference signal (This is further explained in section 2). WSI provides an absolute measurement of displacement from zero OPD, there is no 2π phase ambiguity. However, the recorded fringe pattern will be of the same frequency for both positive or negative OPD and, therefore, an assumption has to be made on the sign of the height determined. Since zero OPD occurs at the midpoint of the depth of field, this limits WSI to using only half of the potential instrument measurement range and presents serious issues when no *a-priori* knowledge of the sample exists. One possible solution is to add an offset between the two interferometer arms, in such a way as to move the zero OPD plane outside the depth of field of the objective lens in the measurement arm. However, positions further away from the zero OPD are associated with a decreased visibility of the interference signal, and therefore a lower signal to noise ratio (SNR). This leads to increased measurement noise which becomes significant for objectives with large depths of field.

In this paper it is demonstrated how to solve the sign ambiguity based on the acquisition of only two WSI signals in quadrature (hereafter, referred to as quadrature WSI (Q-WSI)) whilst working where the visibility of the interference is at its maximum. The problem was solved employing four mechanical phase shifts by Kato et al. [15]. In our case an *a-priori* knowledge of the signal background and correction due to its non-perfect removal allow one to employ only two phase shifts. This technique eliminates the limitation around the position at zero frequency of the standard WSI keeping the number of phase shifts to its minimum. Enabling one to distinguish positive and negative OPDs and allowing measurement around the zero OPD has the effect of more than doubling the measurement range of the instrument without affecting the measurement speed.

In section 2, the optical setup of the instrument is discussed and the phase demodulation algorithms for both the standard WSI method and the proposed Q-WSI method are explained. Performance simulations are presented in section 3. In section 4, a model for the possible sources of error for the Q-WSI method is derived. In section 5 experimental measurements are shown to demonstrate the Q-WSI technique. Finally, in section 6, real surface measurements are presented for both algorithms and the improvements discussed. In section 7, a derivation of the Cramer-Rao bound (CRB) for both methods is discussed for a performance comparison in the presence of Gaussian additive noise.

2. INTERFEROMETER DESIGN AND THEORY

The WSI instrument setup used can be divided into three major blocks (see Figure 1): the light source, the interferometer and the control electronics. The light coming from a white light halogen bulb is collimated and filtered by an acousto-optic tuneable filter (AOTF). By changing the vibration frequency of the AOTF crystal, only one wavelength is selected and coupled into the fibre. The light delivered from the fibre is collimated into a Linnik interferometer. For Q-WSI, the reference mirror is mounted on a piezoelectric actuator that is controlled via a digital acquisition board (DAQ). The light reflected by the reference mirror and the sample recombines producing an interference signal that is imaged on the CCD camera. In the standard WSI measurement process, the reference mirror is fixed and a frame is acquired by the CCD camera for each selected wavelength.

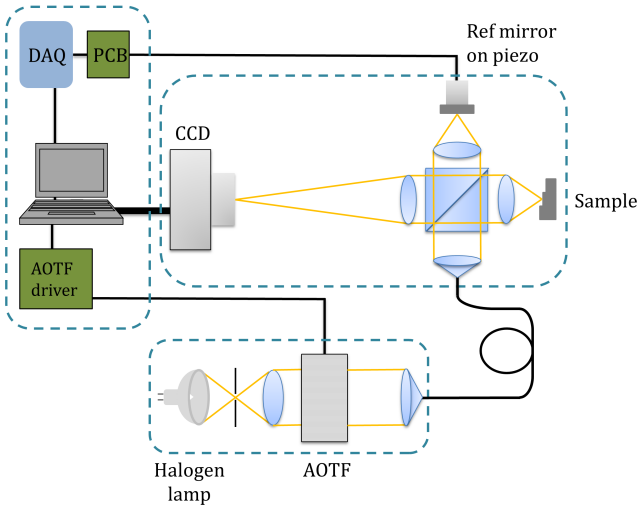

Fig. 1. WSI setup. Top left block: control and computing electronics. Bottom block: wavelength sweeping light source by means of an acousto-optic tuneable filter (AOTF). Top right: Linnik type interferometer.

The intensity of the interference pattern obtained by the WSI for a pixel at position (x, y) in the instrument field of view can be expressed by:

$$I(x,y,k) = q(k) + V(k)\cos[4\pi k(z_m(x,y) - z_r(x,y))] \quad \textbf{(1)}$$

where k is the wavenumber of the interfering light (inverse of the wavelength $\frac{1}{\lambda}$), $q(k)$ is the signal background, and $V(k)$ is the fringe visibility; $2(z_m(x,y) - z_r(x,y))$ is the OPD between the measurement and reference arm. For the following derivation, $z_r(x,y)$ is assumed the position of the reference mirror while not moving, therefore, set equal to zero. For clarity the spatial dependence of the OPD is not explicty shown, as the same computation is made for all pixel in the instrument field of view. As the wavenumber is scanned, the phase shift introduced is proportional to the surface position (z_m); therefore, by demodulating the phase and extracting the fringe pattern frequency, it is possible to infer the surface height. The algorithm employed to demodulate the phase from the fringe pattern is that described by Takeda et al.[16], and is summarised below. For the following derivation the mean background $q(k)$ and the cosine amplitude modulation $V(k)$ are removed by subtraction and normalisation, respectively. A fringe pattern can, therefore, be rewritten according to the Euler formula for the cosine as

$$\frac{I(k) - q(k)}{V(k)} = \frac{1}{2}[\exp(i4\pi k z_m) + \exp(-i4\pi k z_m)] \quad \textbf{(2)}$$

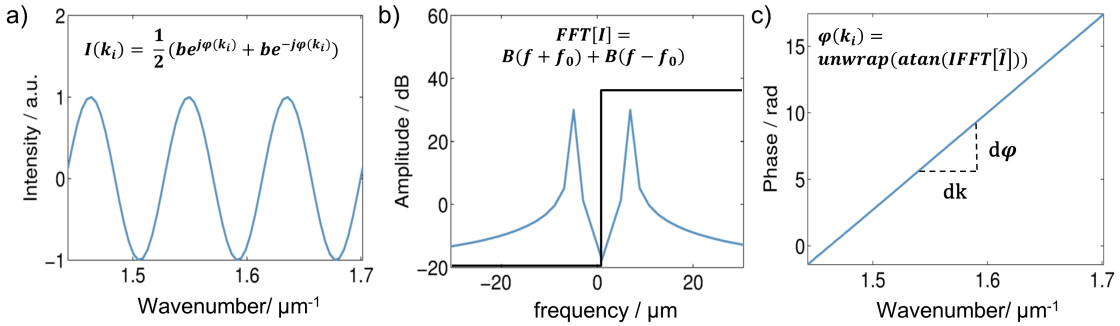

Fig. 2. WSI algorithm for phase demodulation: simulated interference pattern with background removed and visibility normalised (a); Fourier Transofrm of the interference pattern and ideal filter transfer function to separate the two peaks (b). Note that for low frequency the peak become closer making filtering problematic. Demodulated phase whose slope provide an estimation of the OPD (c).

where z_r is considered equal to zero (a simulated fringe pattern is shown in Figure2(a)). The two phasors correspond to the positive and negative frequency peaks in the Fourier transform. Half the spectrum is filtered out to select only one of those two peaks (see Figure2(b)). The filtered spectrum is then inverse-Fourier-transformed. Depending on which peak is selected, an important assumption is made: the measured z-position (z_m) is assumed positive or negative; therefore, fringe patterns with higher frequency are interpreted as either peaks or valleys in the surface topography based on this assumption. The inverse Fourier transform of the filtered spectra ($\hat{I}(k)$) is only one of the terms in Eq. 2. By applying a arctangent function it is possible to extract the phase

$$\varphi(k) = \arctan \hat{I}(k). \tag{3}$$

The obtained phase is known modulo 2π and, therefore, an unwrapping step is necessary. The phase is unwrapped by adding 2π phase at the discontinuities (see Figure2(c)). Lastly, a linear fitting step allows the estimation of the frequency and, therefore, the z-position from the phase slope

$$z_m = \pm \frac{1}{4\pi} \frac{\Delta\varphi}{\Delta k} \tag{4}$$

where $\frac{\Delta\varphi}{\Delta k}$ is the phase slope. The phase slope calculated can be either positive or negative depending on which Fourier peak corresponding to the cosine is selected and therefore its sign is based on an *a-priori* assumption. The effect of a wrong assumption has the effect of mirroring the surface topography, *i.e.* the surface peaks are measured as valleys and vice versa. Some surface parameters such as the root mean square roughness (S_q) are not affected by such an error, but parameters which can be positive or negative, such as skewness (S_k) would report an erroneous sign. To eliminate the z-position sign ambiguity, a further wavelength scanning measurement can be taken in order to obtain two interference patterns in quadrature and interpret them respectively as the real and imaginary axis to describe a complex signal. The real part is the same as in Eq. 1, with $z_r = 0$. The imaginary part is obtained by introducing a phase shift in the reference arm as a function of wavelength by simply shifting the reference mirror at each scan step, in order to have the same frequency as the real part, but with a constant phase shift of $\pi/2$ (the so-called quadrature condition). Thus the condition on the amount of spatial translation of the reference mirror is

$$4\pi k z_r = -\pi/2 \tag{5}$$

Inverting Eq. 5 gives the amount of displacement for the reference mirror as a function of wavelength

$$z_r(k) = -\frac{1}{8k} \tag{6}$$

Rewriting the interference pattern as a sum of the real and imaginary parts after background subtraction and amplitude normalisation gives

$$\begin{aligned} I_{complex}(k) = \cos(4\pi k z_m) + i\cos(4\pi k z_m - \pi/2) = \\ \cos(4\pi k z_m) + i\sin(4\pi k z_m) = \exp(i4\pi k z_m) \end{aligned} \tag{7}$$

Eq. 7 describes a complex signal that rotates clockwise or counter-clockwise depending on whether the measured z_m is negative or positive: the direction of the rotation specifies whether the fringe pattern frequency is positive or negative. Additionally, in the complex signal case, the phase can be extracted directly from the complex recorded signal, as in Eq. 3, whilst in the standard WSI a phase demodulating algorithm needs to be employed to separate the two phasors corresponding to the cosine term. Sequentially, the phase is unwrapped and a linear fit allows the phase slope to be estimated and the z-position to be determined as in Eq. 4 without any assumption on the sign of the estimated z-height.

3. INTERFEROMETER SIMULATIONS

In the measurement the surface height is estimated from N observations of the interference pattern. Our observational model perturbed by additive random noise is given by

$$I_n(\boldsymbol{\alpha}) = S_n(\boldsymbol{\alpha}) + W_n \qquad n \in [0, ..., N-1] \tag{8}$$

where $I_n(\boldsymbol{\alpha})$ is the n-th observation data, $S_n(\boldsymbol{\alpha})$ is the modelled ideal system response for the n-th wavenumber, $\boldsymbol{\alpha}$ is the vector of unknown parameters and W_n is the random additive noise. For the standard WSI case the ideal system response is:

$$S_n(\boldsymbol{\alpha}) = b\cos(4\pi k_n z_m) \tag{9}$$

where k_n is the n-th wavenumber and z_m is the z-position to estimate. On the other hand, the system response for the Q-WSI is:

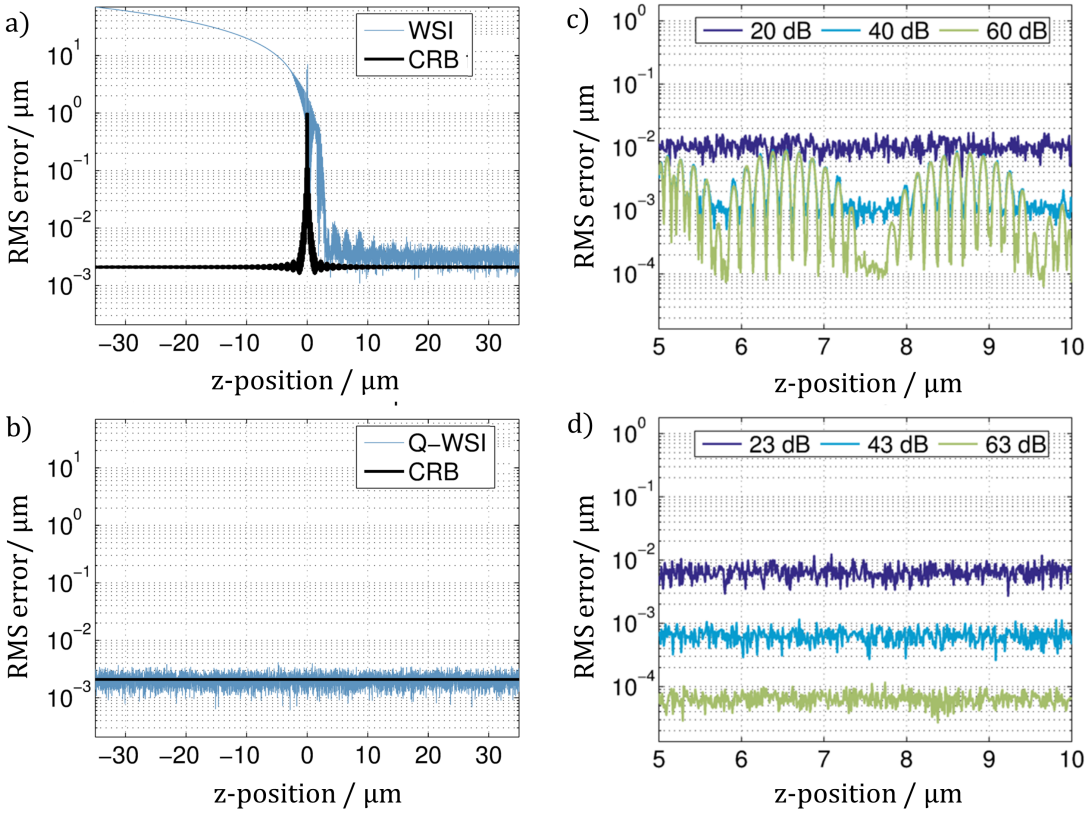

Fig. 3. Comparison of the algorithms response with 256 total samples. Real interference pattern algorithm response with a SNR of 30 dB (a), complex interference pattern algorithm response with a SNR of 33 dB (b). The black line is the Cramer-Rao bound.Comparison of real WSI (c) and complex Q-WSI (d) methods in terms of RMS error for a positive range of heights at three representative SNRs

$$S_n(\boldsymbol{\alpha}) = b\exp(i4\pi k_n z_m). \tag{10}$$

where the signal has been modelled by a complex phasor. For a given additive noise amplitude and therefore for a specific SNR, the variance in the fringe pattern frequency estimation due to additive noise (also called the Cramer-Rao Bound, CRB, and its square root, the root mean square error RMSE) can be calculated for both cases. Details of how to calculate the RMSE are reported in section 7 and hereby the main result is reported: in the WSI case, the RMSE is a function of the number of periods in the recorded fringe pattern, with increasing sensitivity to fringe pattern with less then 2 periods, *i.e.* closer to the zero OPD. On the other hand, in the Q-WSI case the RMSE is insensitive to the number of periods in the recorded fringe pattern, but it is only a function of the SNR.

In this section, simulations of the algorithm RMSE for both the standard WSI and proposed Q-WSI method are presented. The system response is simulated with Eq. 21 and 23 for a given z-position. White independent Gaussian noise is added to the ideal system response in order to achieve a desired ratio between the sinusoid amplitude and the noise standard deviation ($\frac{b}{\sigma}$). For a real sinusoidal signal, the power is $\frac{b^2}{2}$, whilst for a complex sinusoidal signal, it is b^2. Therefore, the signal to noise ratio is 3 dB higher in the Q-WSI case. Ten different noise patterns were generated and the RMSE of the estimated z-position through the frequency is calculated. For consistency in measurement time, the WSI and Q-WSI are simulated with the same total number of measured points: the WSI pattern is sampled in N points, while the Q-WSI has $N/2$ samples for the real part and $N/2$ samples for the complex part, i.e. the sampling density is less in the Q-WSI case. The Nyquist-Shannon theorem is satisfied in both cases.

Figure 3(a) and Figure 3(b) show the algorithm response for the WSI and Q-WSI cases in terms of the RMSE of the z-position estimation. In the WSI case (Figure 3(a)), z-position measurements are possible only in half of the instrument's potential measurement range. Also, there are periodic non-linearities in the system response with increasing amplitude closer to the zero height (zero OPD point), and there is a CRB singularity at the zero z-position. This error is in agreement with the results discussed in Moschetti et al [17]. Figure 3(c) shows a zoomed version of Figure 3(a) for several values of signal SNR. The RMSE is constant across the range for a SNR up to 20 dB with a RMSE of 10 nm. For a SNR above 20 dB the algorithm response non-linearity start to have a contribution larger than the RMSE due to the additive noise, becoming the main contribution. In contrast, for the Q-WSI case (see Figure 3(b)) it is possible to exploit the full vertical range of the instrument and the algorithm response does not show significant non-linearity. Additionally, the RMSE scales with the SNR (see Figure 3(d)), and it is not limited by the algorithm non-lineairty as in the WSI technique.

4. ERROR SOURCE

A real interference signal is affected by distortion such as an offset not equal to zero, a different amplitude of the real and

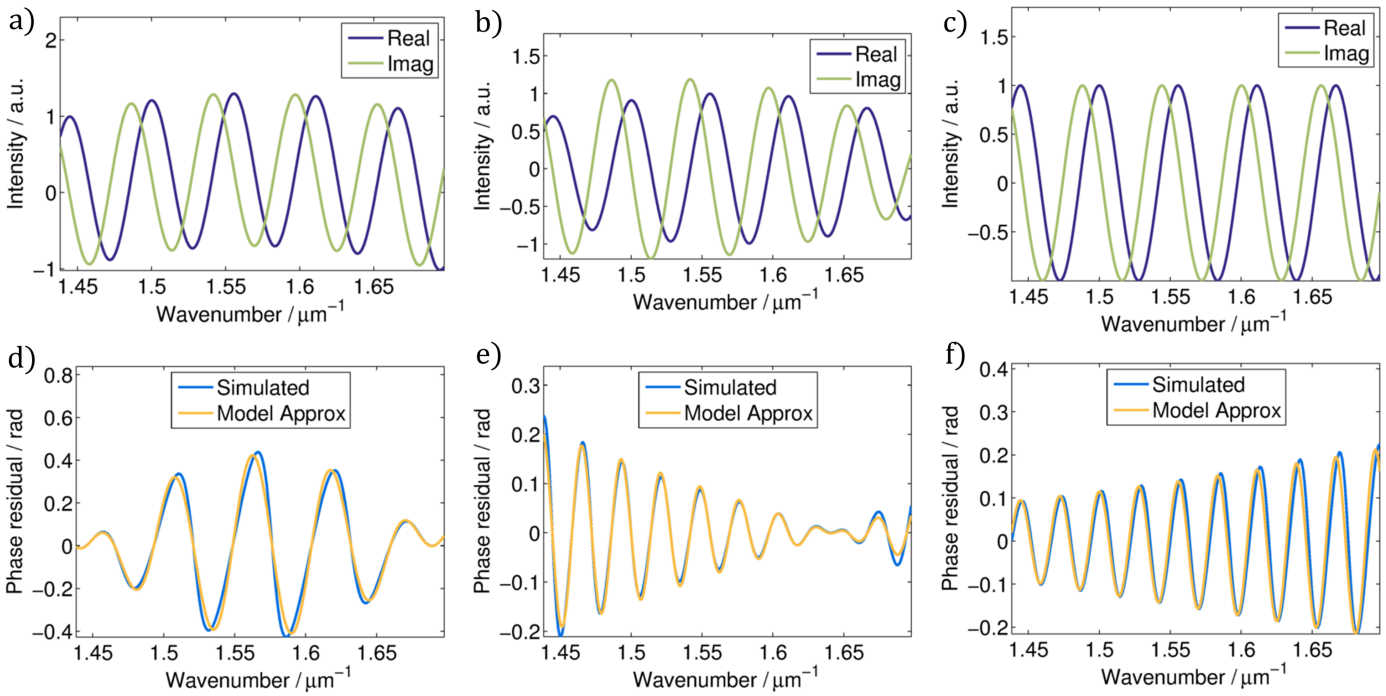

Fig. 4. Effect of error sources in the Q-WSI method. The real and imaginary components of the interference signal are shown (top row) for three cases: non-zero mean (a), different envelope amplitudes (b), and piezo phase shift error (c). The relative phase distortion from the ideal linear case is plotted (bottom row) from the simulation and according to the approximated linear model relative to the mean (d), envelopes (e) and actuator (f).

imaginary component and lack of quadrature [18]. In traditional interferometric systems the signal mean and the amplitudes are constant due to use of a single wavelength (usually a laser). In WSI, the background and the fringe amplitude are a function of the wavenumber (k) due to the different transmission of the optical component at different wavelengths. Additionally, the phase change upon reflection of the light from the sample and the reference mirror may cause a distortion of the phase and therefore the phase distortion is a function of the wavenumber as well.

In general, a more realistic interference signal is:

$$\begin{aligned} I_{complex}(k) &= q_{real}(k) + V_{real}(k)\cos(4\pi k z_m) \\ &\quad + i[q_{imag}(k) + V_{imag}(k)\cos(4\pi k(z_m - z_r))] \end{aligned} \tag{11}$$

where $q_{real}(k)$ and $q_{imag}(k)$ are the mean intensity function of the real and imaginary components respectively, and $V_{real}(k)$ and $V_{imag}(k)$ the interference envelope functions which are both a slowly-varying function of k. The z-axis actuator calibration errors are modelled by substituting $z_r(k) = -\frac{1}{8k} + P(k)$, where $P(k)$ takes into account the lack of quadrature. Substituting in Eq. 11 and using trigonometric identities leads to

$$\begin{aligned} I_{complex}(k) &= q_{real}(k) + V_{real}(k)\cos(4\pi k z_m) \\ &\quad + i\big[q_{imag}(k) + V_{imag}(k)[\sin(4\pi k z_m)\cos(4\pi k P(k)) \\ &\quad + \cos(4\pi z_m)\sin(4\pi k P(k))\big] = C(k) + iS(k) \end{aligned} \tag{12}$$

where the ideal system response is obtained by assuming $q_{real}(k) = q_{imag}(k) = 0$, $V_{real}(k) = V_{imag}(k)$ and $P(k) = 0$. The relative phase is then given by

$$\Theta(k) = \arctan\left[\frac{S(k)}{C(k)}\right] \tag{13}$$

which, in the ideal case, is perfectly linear. The phase deviates from a perfect linear distribution due to signal non-ideality (offset, envelope and phase shift error). The distortion of the phase due to those effects can be obtained analytically by linearising the model around the ideal system response

$$\begin{aligned} \Theta(k) &= \Theta_0(k) + \frac{\partial\Theta}{\partial q_{real}} q_{real}(k) + \frac{\partial\Theta}{\partial q_{imag}} q_{imag}(k) \\ &\quad + \frac{\partial\Theta}{\partial V_{real}} V_{real}(k) + \frac{\partial\Theta}{\partial V_{imag}} V_{imag}(k) + \frac{\partial\Theta}{\partial P} P(k). \end{aligned} \tag{14}$$

Analytically we can obtain

$$\begin{aligned} \Theta(k) &= 4\pi k z_m - q_{real}(k)\sin(4\pi k z_m) + q_{imag}(k)\cos(4\pi k z_m) \\ &\quad + [V_{imag}(k) - V_{real}(k)][\frac{1}{2}\sin(2 * 4\pi k z_m)] \\ &\quad + 4\pi k P(k)[\frac{1}{2} + \frac{\cos(2 * 4\pi k z_m)}{2}] \\ &= 4\pi k z_m + r(k). \end{aligned} \tag{15}$$

In effect, the ideal linear varying phase is distorted with added ripples. Those ripples have amplitude proportional to the functions expressing the means ($q(k)$), envelopes ($V(k)$) and phase errors ($P(k)$). The mean offset components (q_{real} and q_{imag}) leads to a ripple with the same frequency as the interference signal ($4\pi k z_m$). The envelopes (V_{real} and V_{imag}) add a ripple with a frequency twice that of the fringe pattern frequency ($2 * 4\pi k z_m$).

Finally, the actuator phase shift error adds a ripple with twice the fringe pattern frequency ($2 * 4\pi k z_m$) and a constant bias ($kP(k)$). Figure 4 shows examples of those errors, and compares the simulated phase ripples with the approximate model derived above. In Figure 4(a), two simulated interference patterns in quadrature with a quadratic background ($q(k) = q_0 + q_1(k - k_c)^2$, with q_0 equal to 30 % the fringe visibility and a quadratic drop towards the edge of the signal window) are shown. In Figure 4(d) the residual of the phase after a least-squares linear fit are shown and compared with the approximation in Eq. 15. The maximum amplitude of the phase ripple is 0.433 radians and is in agreement with the approximated model. In Figure 4(b) two interference patterns in quadrature with different envelopes (20 % amplitude difference with quadratic drop towards the edge and a shifted maximum by 0.05 μm^{-1}), are shown. The phase residuals are in agreement with the approximation model and the maximum phase error is 0.238 radiant (Figure 4(e)). For the phase shift errors, a constant offset error of 10 nm and a linear error of 10 % between the quadrature interference components are simulated in Figure 4(c). The phase ripple has a maximum amplitude of 0.225 radiants and agrees with the approximated model (Figure 4(f)). These phase distortions due to the above interference signal non-idealities cause a bias in the linear fitting of the phase slope and therefore introduces error in the measurement, usually called ripple-error or fringe bleed-through [19]. In practical application, the backgrounds and amplitudes of the quadrature components depends on the power of the light source for each wavenumber and their expression can be estimated *a-priori* and corrected by fitting the approximated model to the demodulated phase. On the other hand, the phase error of the quadrature components is affetected by the calibration errors of the actuator but also by the phase change upon reflection and enviromental vibrations. Further correction of the phase errors is outside the scope of this paper.

5. EXPERIMENTAL RESULTS

Two surfaces have been measured in order to evaluate the measurement performance of the proposed Q-WSI method in a real instrument, a step height and an optical flat. As previously discussed, the main advantage of Q-WSI over the standard WSI technique is that it is able to distinguish between positive and negative z-positions. A step height with a nominal value of 30 µm is measured across the zero z-position plane. Figure 5 shows the surface topography measurement and the corresponding ISO-5436 [20] step height analysis for both the standard WSI (Figure 5(a)) and Q-WSI methods (Figure 5(b)). The step heigh measurement with the standard WSI technique is folded, due to the erroneous assumption on the sign of the measured OPD. The top and bottom plane of the step height are measured respectively at an absolute position (with the assumption of a negative sign) of approximately -14.6 µm and -15.3 µm. Therefore, a step height with a mean value of 0.7223 µm is measured compared with a calibrated value given by a traceable contact stylus instrument (29.864 µm $\pm$ 0.116 µm at k = 2). On the other hand, for the Q-WSI technique (Figure 5(b)), the sign of the OPD is resolved and the top and bottom plane are measured respectively at a position of approximately +14.6 µm and -15.3 µm, leading to an estimated step height value of 29.800 µm, a value within the uncertainty of the contact stylus traceable measurement.

Another advantage of the Q-WSI technique is its ability to estimate z-positions around the zero OPD point. Figure 6 shows the measurement of a tilted optical flat across the zero z-position plane by both the standard WSI and the Q-WSI methods. The standard WSI technique begins to display significant error for z-positions in the range between $\pm$ 3 µm. In this range, the surface is not correctly measured and shows surface spikes with an amplitude of approximately 2 µm, plus a folded shape due to the OPD sign assumption. The Q-WSI method improves the measurement in this region: it measures the z-positions in this range correctly resolving the sign ambiguity. A residual surface waviness with an amplitude of approximately $\pm$ 150 nm is visible. This waviness is due to phase distortion caused by the phase errors, described in section 4, which causes a deviation from a perfect linear behaviour of the z-axis. The z-axis non-linearity amplitude can be reduced by an order of magnitude by combining the frequency and phase information of the fringe pattern [21].

The same tilted optical flat is also measured further away from the zero OPD to compare the z-axis non-lineairty coefficient with the WSI and Q-WSI technique. In Figure 7 the measurement results are shown with the tilt removed. Ripple in the direction of surface tilt is visible due to phase shift errors. The error is reduced in the Q-WSI technique to $\pm$ 20 nm from an initial value of $\pm$ 40 nm with the standard WSI technique. The error is readuced due a simplified phase demodulation procedure which removes the additional bias caused by the spectral leakage [17].

The extended measurement range comes at the cost of a reintroduced mechanical scan. However, in our setup, the mechanical scanning reintroduced does not affect the measurement speed which is set by the CCD camera frame rate. For high-speed cameras, the mechanical scaning can be completely avoided by capturing two or more phase shifts in a single shot employing multiple cameras [24] or a phase-shifts pixelated mask [23]. However, in the case of a phase-shifts pixelated mask, additional polarisation optics are required and errors might arise from object dependent polarisation effects and the mask's dependency on the wavelength and polarisation of the light. In our experimental setup, with a 5× objective lens it is possible to acquire data for heights up to 70 µm in approximately 1.28 seconds, mainly limited by the CCD camera speed (200 fps). For comparison, a CSI acquisition of surface with heights up to 70 µm, at a sub-Nyquist scan rate of 350 nm per frame [22] and same camera speed would take 1 seconds.

6. CONCLUSION

In conclusion, a Q-WSI method has been proposed and simulation and experimental results confirm its validity. Compared to the standard WSI method, the Q-WSI method is able to exploit the whole fringe visibility range available to the WSI technique by employing an additional phase shift. Specifically, the method can distinguish between positive and negative z-positions, effectively doubling the instrument's working range. Moreover, the method is capable of measuring z-positions from fringe data containing less than a period, i.e. the short range spanning across zero OPD is now accessible. Furthermore, the method significantly reduces the non-linearities in the instrument's vertical axis due to the processing algorithm. Algorithm vertical axis non-linearities due to signal non-ideality are still evident as a small ripple and a model is proposed to account for these. Despite the fact that some mechanical scanning is reintroduced, the mechanical scan does not slow down the measurement which is limited by the CCD camera. The Q-WSI technique described here, combined with the improvement published in [21] allows to exploit the entire dynamic range of the WSI technique.

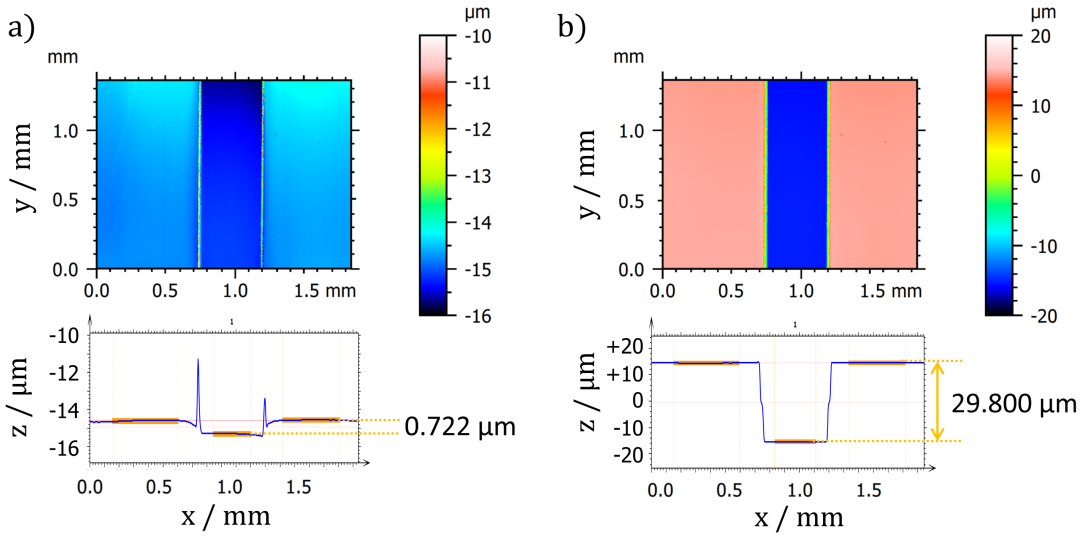

Fig. 5. A step height of nominal height 30 µm as measured with a) standard WSI and b) Q-WSI methods. The profiles are the vertical average of the areal measurement and the step height is evaluated according to the ISO-5436 procedure.

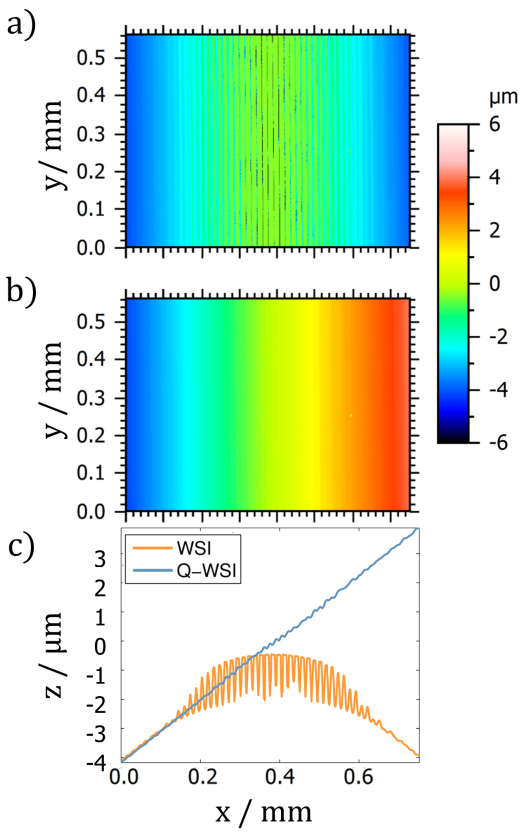

Fig. 6. Comparison of tilted optical flat across the zero height measured with standard WSI (a) and Q-WSI (b). In (c) the averaged horizontal profiles of the measurement on the left are compared.

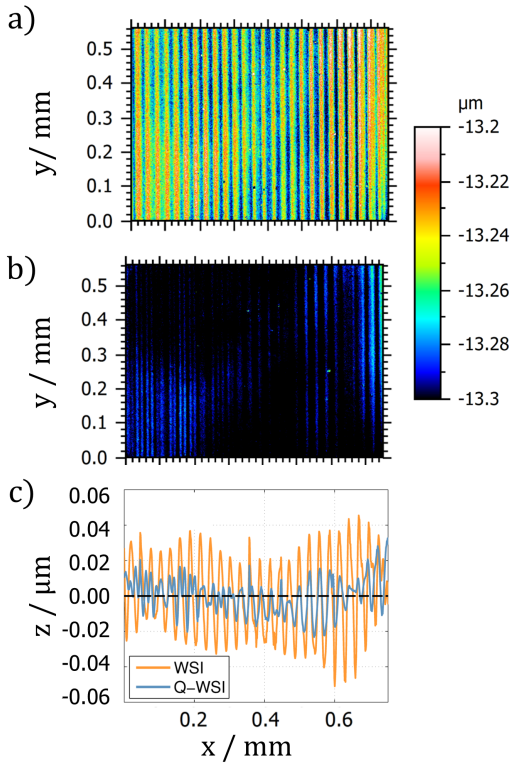

Fig. 7. Comparison of tilted optical flat measured with standard WSI (a) and Q-WSI (b) away from the zero height position. The surfaces are levelled and plotted on the same scale to show the vertical axis non-linearity differences. A comparison of the averaged horizontal profiles of the surfaces is shown in (c).

7. APPENDIX A: CRAMER-RAO BOUND DERIVATION

In the measurement the surface height is estimated from N observations of the interference pattern. Our observational model perturbed by additive random noise is given by

$$I_n(\boldsymbol{\alpha}) = S_n(\boldsymbol{\alpha}) + W_n \qquad n \in [0, ..., N-1] \tag{16}$$

where $I_n(\boldsymbol{\alpha})$ is the n-th observation data, $S_n(\boldsymbol{\alpha})$ is the modelled ideal system response for the n-th wavenumber, $\boldsymbol{\alpha}$ is the vector of unknown parameters and W_n is the random additive noise. For a given set of $\{k_n\}_{n=0}^{N-1}$, $S_n(\boldsymbol{\alpha})$ describes an N-dimensional model surface in R^p, where p is the number of parameters in the vector $\boldsymbol{\alpha}$. The observed data vector $I(\boldsymbol{\alpha})$ is as a perturbation from the system's ideal response $S(\boldsymbol{\alpha})$, where $\boldsymbol{\alpha}$ describes the true state of the system. In matrix form, the problem in Eq 16 can be written as

$$\begin{aligned} \boldsymbol{I} &= \boldsymbol{S}(\boldsymbol{\alpha}) + \boldsymbol{W} \\ \boldsymbol{W} &= \sigma^2 \mathfrak{I} \end{aligned} \tag{17}$$

where $\mathfrak{I}$ is the identity matrix and σ^2 is the variance of the additive noise. Eq. 17 is valid under the assumption that that the random effects in the observed data are independent. If the system response is linear, then $\boldsymbol{S}(\boldsymbol{\alpha})$ is a linear function of the parameters α, and the maximum-likelihood estimation method is the least-square[25]. Furthermore, if the estimation is unbiased, it is possible to propagate $\boldsymbol{W}$ through, to obtain the uncertainty matrix $\boldsymbol{W_{LS}}$ associated with the least square estimate $\boldsymbol{\alpha_{LS}}$. If the system response $\boldsymbol{S}(\boldsymbol{\alpha})$ is not linear, the estimator not biased and the perturbation sufficiently small, we can still linearise the problem around the solution $\boldsymbol{\alpha_{LS}}$ to determine an approximate uncertainty matrix [25]

$$\boldsymbol{W_{NL}} \approx \sigma^2 [\boldsymbol{J}^T \boldsymbol{J}]^{-1} \tag{18}$$

where $\boldsymbol{J}$ is the Jacobian matrix of the system response at the solution α_{NL} defined as

$$J_{nj} = \frac{\partial S(k_n, \boldsymbol{\alpha_{NL}})}{\partial \alpha_j}, \qquad n \in [0, ..., N-1] \tag{19}$$

This result is also known as the Cramer-Rao bound (CRB). This CRB establishes a lower bound on the variance of the estimation of a deterministic parameter from measured data with additive noise [26]. The CRB is a known result in the signal processing field both for real and complex tone estimation [27]. For clarity, the CRB is adapted for the case in which the frequency, the amplitude and the phase are the unknown parameters and the frequency has to be estimated to infer the surface z-position.

For the real fringe pattern algorithm (standard WSI) the system response is

$$\begin{aligned} S(k_n, \boldsymbol{\alpha}) &= b \cos(4\pi k_0 z_p + 4\pi(k_n - k_0) z_f) \\ &= b \cos(\varphi_n) \qquad n \in [0, ..., N-1] \end{aligned} \tag{20}$$

where $\alpha = [b, z_f, z_p]^T$, is the vector of the unknown parameters, and in particular z_f and z_p are the estimated z-positions from the phase and frequency respectively. Applying Eq. 18 and 19 to the particular case of Eq. 20 gives

$$\boldsymbol{W_{WSI}} \approx \sigma^2 \begin{bmatrix} d_{11} & d_{12} & d_{13} \\ d_{12} & d_{22} & d_{23} \\ d_{13} & d_{23} & d_{33} \end{bmatrix}^{-1} \tag{21}$$

where:

$$\begin{aligned} d_{11} &= \sum_{n=0}^{N-1} [\cos(\varphi_n)]^2 \\ d_{22} &= \sum_{n=0}^{N-1} [4\pi b(k_n - k_0) \sin(\varphi_n)]^2 \\ d_{33} &= \sum_{n=0}^{N-1} [4\pi b k_0 \sin(\varphi_n)]^2 \\ d_{12} &= \sum_{n=0}^{N-1} (-4\pi b(k_n - k_0) \cos(\varphi_n) \sin(\varphi_n) \\ d_{13} &= \sum_{n=0}^{N-1} (-4\pi b k_0) \cos(\varphi_n) \sin(\varphi_n) \\ d_{23} &= \sum_{n=0}^{N-1} [4\pi b \sin(\varphi_n)]^2 (k_n - k_0) k_0 \end{aligned}$$

.

The second element on the diagonal in the matrix in Eq. 21 is the variance in the z-position estimation from the frequency due to an additive noise perturbation with variance σ^2. Note that the matrix terms depends on the z-position to estimate from the phase φ_n. Summing the sampled value of a cosine or sine over an integer number of periods would give a lower variance value than summing over samples of a sinusoid with a non-integer number of periods. For the case in which an imaginary fringe pattern is recorded (Q-WSI), the system model is

$$\begin{aligned} S(k_n, \boldsymbol{\alpha}) &= b \exp(4\pi k_0 z_p + 4\pi(k_n - k_0) z_f) \\ &= b \exp(\varphi_n) \qquad n \in [0, ..., N-1] \end{aligned} \tag{22}$$

and, therefore, the propagated variance in the parameters estimation due to a perturbation in the observed data is

$$\boldsymbol{W_{QWSI}} \approx \sigma^2 \begin{bmatrix} N & " & " \\ 0 & \sum_{n=0}^{N-1} [4\pi b(k_n - k_0)]^2 & " \\ 0 & \sum_{n=0}^{N-1} [4\pi b]^2 k_0 (k_n - k_0) & N[4\pi b k_0]^2 \end{bmatrix}^{-1} \tag{23}$$

The variance in the z-position estimation from the frequency is the second diagonal element for both cases. An important difference is that, in the complex case (Q-WSI), the bound is independent from the z-position being estimated.

8. FUNDING INFORMATION

The authors gratefully acknowledge the funding of the EPSRC Centre for Innovative Manufacturing in Advanced Metrology (EP/I033424/1), ERC (ERC-ADG-228117), EU FP7 Nanomend (280581), and the NMS Engineering and Flow Programme 2011-2014.

9. ACKNOWLEDGEMENTS

The authours would like to thank Dr. Mattia Giovanni Lazzerini and Dr. Andrew Henning for useful suggestions to improve the quality of this paper.

REFERENCES

1. R. K. Leach, *Fundamental Principles of Engineering Nanometrology* (Elsevier, 2010).

2. P. De Groot, "Principles of interference microscopy for the measurement of surface topography," Advances in Optics and Photonics **7**, 1–65 (2015).
3. Z. Wang and Y. Jiang, "Wavenumber scanning-based Fourier transform white-light interferometry." Applied Optics **51**, 5512–6 (2012).
4. A. Davila, J. M. Huntley, C. Pallikarakis, P. D. Ruiz, and J. M. Coupland, "Wavelength scanning interferometry using a Ti:Sapphire laser with wide tuning range," Optics and Lasers in Engineering **50**, 1089–1096 (2012).
5. X. Jiang, K. Wang, F. Gao, and H. Muhamedsalih, "Fast surface measurement using wavelength scanning interferometry with compensation of environmental noise," Applied Optics **49**, 2903–2909 (2010).
6. J. A. N. Buytaert and J. J. J. Dirckx, "Study of the performance of 84 phase-shifting algorithms for interferometry," Journal of Optics **40**, 114–131 (2011).
7. M. Servin, J. C. Estrada, and J. A. Quiroga, "The general theory of phase shifting algorithms." Optics Express **17**, 21867–21881 (2009).
8. R. Leach, *Optical Measurement of Surface Topography* (Springer, 2011).
9. I. Yamaguchi, T. Ida, and M. Yokota, "Measurement of Surface Shape and Position by Phase-Shifting Digital Holography," Strain **44**, 349–356 (2008).
10. U. P. Kumar, B. Bhaduri, M. Kothiyal, and N. K. Mohan, "Two-wavelength micro-interferometry for 3-D surface profiling," Optics and Lasers in Engineering **47**, 223–229 (2009).
11. P. De Groot, X. C. De Lega, J. Kramer, and M. Turzhitsky, "Determination of Fringe Order in White-Light Interference Microscopy," Applied Optics **41**, 4571–4578 (2002).
12. Y.-S. Ghim and A. Davies, "Complete fringe order determination in scanning white-light interferometry using a Fourier-based technique," Applied Optics **51**, 1922–1928 (2012).
13. S. Kim, J. Kim, and H. Pahk, "Fringe-Order Determination Method in White-Light Phase-Shifting Interferometry for the Compensation of the Phase Delay and the Suppression of Excessive Phase Unwrapping," Journal of the Optical Society of Korea **17**, 415–422 (2013).
14. M. Suematsu and M. Takeda, "Wavelength-shift interferometry for distance measurements using the Fourier transform technique for fringe analysis." Applied Optics **30**, 4046–55 (1991).
15. J.-i. Kato and I. Yamaguchi, "Phase-Shifting Fringe Analysis for Laser Diode Wavelength-Scanning Interferometer," Optical Review **7**, 158–163 (2000).
16. M. Takeda, H. Ina, and S. Kobayashi, "Fourier-transform method of fringe-pattern analysis for computer-based topography and interferometry," Journal of the Optical Society of America **72**, 156 (1982).
17. G. Moschetti, H. Muhamedsalih, O. Connor, X. Jiang, and R. K. Leach, "Vertical axis non-linearities in wavelength scanning interferometry," in "11th International Conference and Exhibition on Laser Metrology, Machine Tool, CMM & Robotic Performance", Lamdamap 2015, euspen, (2015), pp. 31–39.
18. P. L. M. Heydemann, "Determination and correction of quadrature fringe measurement errors in interferometers," Applied Optics **20**, 3382–3384 (1981).
19. Y.-S. Ghim, A. Suratkar, A. Davies, and Y.-W. Lee, "Absolute thickness measurement of silicon wafer using wavelength scanning interferometer," Proceedings of SPIE **8133**, 1–6 (2011).
20. Geneva: International Organization for Standardization, "ISO 5436-1:2001 Geometrical Product Specifications (GPS) – Surface texture: Profile method; Measurement standards – Part 1: Material measures," Tech. rep. (2001).
21. G. Moschetti, A. Forbes, J. Xiang, R. K. Leach, and D. O'Connor, "Phase and fringe order determination in wavelength scanning interferometry," Optics Express **24** (2016).
22. P. de Groot and L. Deck, "Three-dimensional imaging by sub-Nyquist sampling of white-light interferograms," Optics Letters **18**, 1462–1464 (1993).
23. N. J. . Brock, J. E. Millerd, J. C. Wyant, and J. B. Hayes, "Pixelated phase-mask interferometer", US Patent 7,230,717 B2, (12th June 2007).
24. A. Safrani and I. Abdulhalim, "Real-time phase shift interference microscopy." Optics letters **39**, 5220–3 (2014).
25. F. Pavese and A. B. Forbes, *Data Modeling for Metrology and Testing in Measurement Science*, Modeling and Simulation in Science, Engineering and Technology (Birkhäuser Basel, 2008).
26. H. L. Van Trees and K. L. Bell, *Detection Estimation and Modulation Theory, Part I* (John Wiley & Sons, Somerset, NJ, USA, 2013), 2nd ed.
27. D. C. Rife and R. R. Boorstyn, "Single-Tone Parameter Estimation from Discrete-Time Observations," IEEE Transactions on Information Theory **20**, 591–598 (1974).